Chinese Chemical Letters 33 (2022) 693–702

Contents lists available at ScienceDirect

Chinese Chemical Letters

journal homepage: www.elsevier.com/locate/cclet

Two-dimensional metal-organic framework nanosheet composites: Preparations and applications

Yutian Qin [a,b,1], Yue Wan [b,1], Jun Guo [a,*], Meiting Zhao [b,*]

[a] School of Chemistry, Tiangong University, Tianjin 300387, China
[b] Tianjin Key Laboratory of Molecular Optoelectronic Sciences, Department of Chemistry, Institute of Molecular Aggregation Science, Tianjin University, Tianjin 300072, China

ARTICLE INFO

Article history:
Received 8 June 2021
Revised 1 July 2021
Accepted 4 July 2021
Available online 11 July 2021

Keywords:
Metal-organic framework
2D nanosheet
Composite
Energy conversion
Catalysis
Separation
Biomedicine

ABSTRACT

As emerging two-dimensional materials, metal-organic framework (MOF) nanosheet composites possess many unique physical and chemical properties, thus being expected to be widely applied in gas separation and adsorption, energy conversion and storage, heterogeneous catalysis, sensing as well as biomedicine. In this review, we first introduce the methods for integrating MOF nanosheets with other materials to prepare multifunctional composites. Next, the applications of MOF nanosheet composites in versatile fields are summarized and discussed. We hope this review will be instructive for researchers in the aspects of designs, preparations and applications of MOF nanosheet composites.

1. Introduction

Two-dimensional (2D) materials, in recent decades, have received extensive attentions in the fields of sensing, separation, catalysis, optoelectrical device and biomedicine due to their unique physical and chemical properties [1–4]. Particularly, compared with bulk three-dimensional (3D) materials, 2D materials possess some special characteristics [5–8]. For instance, the ultrasmall thickness and relatively large planar dimension endow 2D materials with larger external surface area and more exposed active sites, which are advantageous in sensing and catalysis applications [9–12]. Meanwhile, the high aspect ratio of 2D materials make them suitable candidates for assembling separation membranes, which enjoy the merits of high feedstock flux and low mass transfer resistance [13,14].

Metal-organic frameworks (MOFs) are a class of novel porous crystalline materials constructed with metal nodes and organic polydentate linkers, which typically have periodic planar or triaxial network structure [15,16]. In general, compared with conventional porous materials (*e.g.*, active carbon and metal oxide), MOFs possess tunable topology and structure, facile functionalization and modification, and even larger surface area and higher pore volume [17–19]. As an emerging type of 2D materials, MOF nanosheets have combined both advantages of MOFs and 2D materials, and achieved lots successes in gas separation and adsorption, energy conversion and storage, catalysis, sensing as well as biomedicine [20–26].

In order to further extend the application scope or improve the performance of MOF nanosheets, a series of composites have been proposed by combining MOF nanosheets with other functional components involving metal nanostructures [27–30], inorganic oxides [31,32], graphene [33,34], carbon nanotube (CNT) [35–37], polymers [38,39] and biomacromolecules [40]. The incorporation of other component can modify the physical and chemical properties of pristine MOF nanosheets. For example, carbonized nanomaterials and metal nanoparticles are usually added for improving the electron conductivity of pristine MOF nanosheets; while flexible nanomaterials (*e.g.*, graphene and CNT) are introduced aim at strengthening the mechanical properties of resulting composites [36,41]. In addition, other functional moieties, such as active sites are employed for promoting the catalysis and sensing performances [42]. Consequently, MOF nanosheet composites can usually exert better and even exceptional performance beyond each individual component in versatile application fields [43,44]. In this review, we aim to give a brief overview on the research progress of

* Corresponding authors.
E-mail addresses: junguo@tiangong.edu.cn (J. Guo), mtzhao@tju.edu.cn (M. Zhao).
[1] These authors contributed equally to this work.

https://doi.org/10.1016/j.cclet.2021.07.013
1001-8417/

2D MOF nanosheet composites. First, the preparation methods of MOF nanosheet composites are introduced. Next, the applications of MOF nanosheet composites in diverse fields are discussed. Finally, our personal perspectives on the future development of this field are also provided. We hope these can be instructive for readers who are interested in the rational design and controllable construction of high-performance MOF nanosheet composites for desired applications.

2. Preparations of MOF nanosheet composites

During the past few years, many methods have been developed for the preparation of MOF nanosheets, including bottom up synthesis [45–51] and top down exfoliation methods [52–56]. These methods have been comprehensively summarized in other reviews [57–61]. Herein, we will focus on the preparation of MOF nanosheet composites, which are classified into two groups: supporting/growing other materials on MOF nanosheets, and growing MOF nanosheets on other materials.

2.1. MOF nanosheets as supporters

Metal nanoparticles (NPs), in many occasions, can endow materials with good catalytic activities as well as modified physical and chemical properties [62–65]. Hence, much efforts have been devoted to develop methods for the growth of metal NPs (*e.g.*, Au [66,67], Ag [67,68], Pt [67,69], Pd [69-71], Ru [72,73], Ir [74] and their alloys [67]) on MOF nanosheets [75]. Generally, metal NPs can be deposited by adding metal precursors into the suspension of MOF nanosheets and subsequent reduction treatment. For example, our group has reported the preparation of Au NPs decorated Cu-TCPP(M) nanosheets (TCPP = tetrakis(4-carboxyphenyl)porphyrin; M = Fe, Co). In a typical experiment, $HAuCl_4$ was added to the aqueous suspension of Cu-TCPP(M), and then the obtained mixture was treated with $NaBH_4$. Finally, Au NPs were homogeneously formed on Cu-TCPP(M) with a small dimension of 2.1 ± 0.5 nm [66].

Single-metal sites installed MOF composites have attracted great interests recently, especially in the field of heterogeneous catalysis, as the separately dispersed single-metal sites can exhibit superb activity and selectivity [76]. 2D MOF nanosheets featured with large external surface area and abundant metal-anchoring sites are considered as ideal supporters for installation of single-metal sites. For example, post-synthetic modification strategy was employed in the metallation of 2D $Zr_{12}O_8(\mu_3\text{-}OH)_8(\mu_2\text{-}OH)_6(BPDC)_9$ (denoted as Zr_{12}-BPDC; BPDC = biphenyl-1,1′-dicarboxylate) MOF. In a typical process, $LiCH_2SiMe_3$ was added into the dispersion of pristine Zr_{12}-BPDC to deprotonate the $Zr_{12}O_8(\mu_3\text{-}OH)_8(\mu_2\text{-}OH)_6$ clusters as the first step. Then, as-deprotonated MOF was treated with $Cu(CH_3CN)_4BF_4$ solution for the incorporation of Cu sites to form the final Zr_{12}-BPDC-Cu composite [77].

It is also appealing to integrate metal sulfides with 2D MOF nanosheets [78–80]. Dating back to 2016, our group reported the sulfidation of Co-based MOF nanosheets under 650 °C at the cost of collapse of MOF crystallinity [81]. To resolve this issue, we have further developed a mild preparation method for the incorporation of metal sulfide onto 2D MOF nanosheets. In brief, an ethanol (or aqueous) dispersion of 2D MOF (*e.g.*, M-TCPP, M = Cd, Cu, Co) nanosheets containing organic sulfur source (*e.g.*, thioacetamide, TAA) was heated at mild temperature (*e.g.*, 70 °C for Cd-TCPP, 75 °C for Cu-TCPP, 150 °C for Co-TCPP). Corresponding metal sulfide NPs were formed on the M-TCPP nanosheet surface without altering the 2D morphology substantially (Figs. 1a-c). More importantly, the dimensional size of resultant metal sulfide NPs can be readily regulated *via* adjusting the heating time [82].

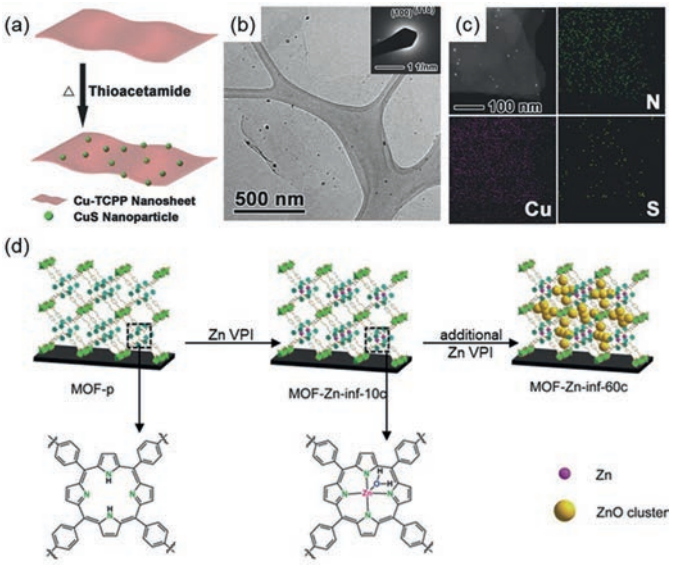

Fig. 1. (a) Scheme of preparation, (b) transmission electron microscopy (TEM) image, (c) dark-field scanning transmission electron microscope (STEM) image and energy-dispersive X-ray spectroscopy (EDS) mapping of CuS/Cu-TCPP composite nanosheets. Reproduced with permission [82]. Copyright 2016, Wiley-VCH. (d) Incorporation of Zn species to 2D $Al_2(OH)_2$(TCPP) MOF. Reproduced with permission [85]. Copyright 2020, Wiley-VCH.

The incorporation of metal oxide into 2D MOF nanosheets can be realized *via* the vapor-phase infiltration (VPI) technology. In a general VPI process, the vapor of metal precursors (*e.g.*, organometallic compounds) are allowed to diffuse into MOF pores for forming desired metal oxide inside MOF after further chemical reactions [83]. Taking an example, a thin layer of $Al_2(OH)_2$(TCPP) was formed onto the carbon fiber first *via* treating the alumina-coated carbon fiber with TCPP solution [84]. Next, as-prepared $Al_2(OH)_2$(TCPP) was placed in an atomic layer deposition (ALD) chamber, and the vapor of diethylzinc and water was introduced alternately. The Zn atom was first incorporated *via* coordination to the N atoms of porphyrin. As the infiltration cycle increased, excessive Zn atoms formed ZnO clusters inside the MOF pores for the fabrication of the final composite (Fig. 1d) [85]. Besides, co-precipitation method can also be used for the incorporation of metal oxide into MOFs. In a representative research, Fe_3O_4 was supported onto Au/Cu(HBTC)-1 nanosheets (*i.e.*, $Cu(HBTC)(H_2O)_3$, BTC = trimesate) with Au NPs pre-deposited. In specification, the mixed solution of $FeCl_2$ and $FeCl_3$ was added into the aqueous dispersion of Au/Cu(HBTC)-1. After being heated for a while, the mixture was adjusted to the alkaline status (pH 10~11) and kept at 80 °C for another 3 h. As a result, Fe_3O_4 NPs with a mean size of 6 nm were formed and anchored onto the hybrid Au/Cu(HBTC)-1 nanosheets [31].

The direct growth strategy can also be utilized for the incorporation of polymers, *e.g.*, polypyrrole (PPy), into MOF nanosheets. In a typical process, pyrrole monomer was mixed thoroughly with an aqueous suspension of Cu-TCPP MOF nanosheets. Owing to the π-π interaction, the monomer molecules were adsorbed onto the MOF surface prior to polymerization. Next, ammonium persulfate was added into the mixture to initiate the polymerization. Finally, Cu-TCPP@PPy composite nanosheets were obtained, in which the surface of Cu-TCPP was covered with a coat of PPy particles uniformly [43].

MOF nanosheets have been used for constructing separation membranes [86–89]. In order to improve the performance of MOF membranes, flexible materials are suggested to be integrated with MOF nanosheets to form composite membranes. A facile graphene

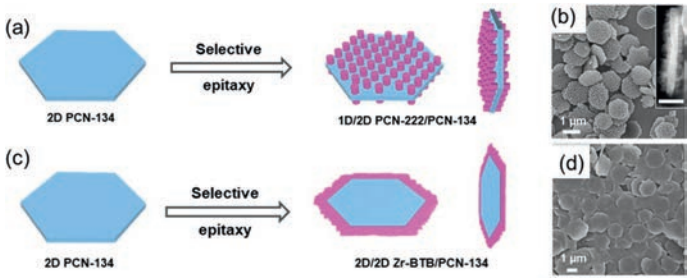

Fig. 2. Scheme of preparation of (a) PCN-222/PCN-134 composite and (c) Zr-BTC/PCN-134 composite. (b) SEM and (Inset) STEM images of PCN-222/PCN-134 composite. (d) SEM image of Zr-BTC/PCN-134 composite. Reproduced with permission [90]. Copyright 2020, American Chemical Society.

oxide (GO) induced method was proposed to construct defect-free MOF membranes with improved mechanical properties. In a typical process, suspension of MOF nanosheets and GO are mixed under sonication assistance, and the obtained mixture is then used to assemble MOF/GO composite membranes on certain substrate through a vacuum filtration device. For example, a uniform CuBDC-GO composite membrane with no visible pinholes or cracks can be obtained through this method, and the assembled composite layer can be firmly adhered to both inorganic and organic substrates (*e.g.*, porous alumina and nylon-6 fiber). It is considered that GO can not only repair the defect by filling the voids between MOF nanosheets, but also form Cu-O bond, hydrogen bond and π-π interaction with CuBDC, thus jointly dramatically improving the separation selectivity of resultant composite membranes [41].

Additionally, 2D MOF nanosheets can be integrated with another type of MOFs, thereby forming MOF-on-MOF composites. Our group has reported a seeded epitaxial growth method for the preparation of MOF heterostructures, in which a type of MOF can grow epitaxially on the surface of another type of MOF seed if their crystalline lattices are matched with each other. For instance, PCN-134, a 2D plate-like MOF constructed by classical Zr_6 clusters and TCPP/BTB (BTB = benzene-1,3,5-tribenzoate) mixed linkers in the *P6/mmm* space group, was synthesized by the solvothermal method in advance. Then, PCN-134 was applied as the seed for epitaxial growth of PCN-222 and Zr-BTB, respectively. PCN-222 is a 1D rod-like MOF constructed by the Zr_6 clusters and TCPP linkers in the *P6/mmm* space group as well. The lattice parameter in the *a-b* plane of PCN-222 is very close to two times of that of PCN-134, and thus, PCN-222 grew vertically on the basal planes of PCN-134 (Figs. 2a and b). In contrast, Zr-BTB possesses a 2D layered structure, and PCN-134 can be regarded as the product of Zr-BTB layers intercalated with TCPP linkers. Since the intralayer coordination bonds of Zr-BTB are much stronger than the interlayer stacking interaction, Zr-BTB are preferable to grow on the edge of PCN-134 (Figs. 2c and d) *via* extension of the intralayer coordination bonds [90].

In another work, a method to integrate different MOF layers *via* Van der Waals force was proposed. As a typical example, Cu-TCPP nanosheets with square lattice (*sql*) topology were combined with Cu-HHTP (HHTP = 2,3,6,7,10,11-hexahydrotriphenylene) nanosheets with the honeycomb lattice (*hyb*) topology. First, the Cu-HHTP layer was formed by spray liquid-phase epitaxial (LPE) growth on the gold substrate. Second, Cu-TCPP nanosheets, prepared *via* direct solvothermal reaction, were dispersed in ethanol and then added drop-by-drop on the surface of water, so as to form a thin film of Cu-TCPP after evaporation of ethanol. Third, the film of Cu-TCPP was transferred onto the Cu-HHTP layer by a stamping procedure. The latter two procedures can be repeated several times, thereby tuning the layers of Cu-TCPP in the resultant composite film [91].

Last but not least, biomacromolecules (*e.g.*, enzyme, protein and nucleic acid) incorporated 2D MOF nanosheets are promising materials in clinical diagnosis and therapy [40,92]. Physical adsorption is a facile strategy to immobilize biomacromolecules onto MOF nanosheets. For example, glucose oxidase can be easily assembled on 2D Cu-TCPP(Fe) nanosheets by mixing the enzyme and corresponding MOF nanosheets in the aqueous medium without impairing the morphology of 2D MOF nanosheets [40].

2.2. Growth of MOF nanosheets on other materials

In contrast to the methods discussed above, MOF nanosheets may also directly grow on other types of materials. For instance, Lin and coworkers reported the growth of 2D MOF nanosheets on CNT [35,36]. In a typical process, carboxylated multiwall CNT was added into the solution containing metal salt and organic ligand (*e.g.*, $HfCl_4$ and Co-metalated 5,15-di(*p*-benzoato)-porphyrin, denoted as CoDBP). After solvothermal reaction, the composite integration of CNT and corresponding 2D MOF nanosheets (*e.g.*, Hf_{12}-CoDBP/CNT) was obtained. Noteworthily, the carboxylate functional groups exposed on CNT were responsible for the adherence of 2D MOF nanosheets onto CNT *via* formation of coordination bonding [36]. Moreover, Qiao *et al.* reported the hybrid nanosheets of Co-BDC MOF and MoS_2. First, MoS_2 were prepared by exfoliation of bulk MoS_2 *via* lithium intercalation. Next, as-prepared MoS_2 layers were mixed with the mixed solution of $CoCl_2$ and H_2BDC. After the mixture being processed under sonication, Co-BDC/MoS_2 hybrid nanosheets were obtained, in which Co-BDC MOF was uniformly formed on the surface of MoS_2 [55]. Besides, the direct growth of 2D MOFs onto metal nanocrystals (NCs) have been reported. For instance, Yang, Yaghi and coworkers prepared nano-Ag⊂MOF composite, in which Ag NCs are enclosed with 2D $Al_2(OH)_2$TCPP MOF. First, an alumina film in thickness of 3 nm was formed onto Ag NCs *via* atomic layer deposition (ALD) using $AlMe_3$ and water as precursors. Next, the as-prepared Al_2O_3-coated Ag NCs were treated with the DMF/H_2O solution containing TCPP ligand under solvothermal conditions, which led to the conversion of Al_2O_3 coating into $Al_2(OH)_2$TCPP MOF layers [93]. Such metal oxide assisted preparation strategy has been further applied to integrate 2D MOF nanosheets with various substrates (*e.g.*, polymer textile and silicon wafer). For example, the ALD step was first carried out to coat an alumina layer onto polypropylene (PP) fiber and silicon wafer (Si/SiO_2), respectively. The obtained materials, *i.e.*, PP@Al_2O_3 and Si/SiO_2@Al_2O_3, were then immersed into the solution containing H_2TCPP ligand and underwent a solvothermal treatment. During which, the Al_2O_3 was able to react with H_2TCPP ligand, thereby forming a layer of $Al_2(OH)_2$(H_2TCPP) MOF (denoted as Al-PMOF) nanosheets onto corresponding substrates, *i.e.*, PP@Al-PMOF and Si/SiO_2@Al-PMOF (Fig. 3a) [84]. In another example, porous alumina tubes were clad in the sheet-shaped zeolitic imidazolate framework (ZIF), $Zn_2(bIm)_4$ (bIm = benzimidazole), *via* dip coating with the ZnO precursor and subsequent treatment with bIm solution to transform ZnO into $Zn_2(bIm)_4$ [86].

The hydroxy double salt (HDS) intermediated method was developed to regulate the orientation of MOF nanosheets in the resultant composites. HDSs are a series of layered materials those consist of two types of divalent metal cations connected with inorganic or organic anions [94]. Typically, a conformal ZnO layer was formed on PP substrate *via* ALD for further use (Fig. 3b). If the produced PP@ZnO composite was directly treated with a mixed solution of $Cu(NO_3)_2$ and TCPP, 2D Cu-TCPP would horizontally grow onto the PP substrate (Fig. 3c). Instead, the HDS-intermediated method led to the radial growth of MOF nanosheets. To be specific, PP@ZnO was first processed with $Cu(NO_3)_2$, and needle-shaped layers of HDS(Zn,Cu) were formed radially as the intermediate; then, a treatment with TCPP was performed to trans-

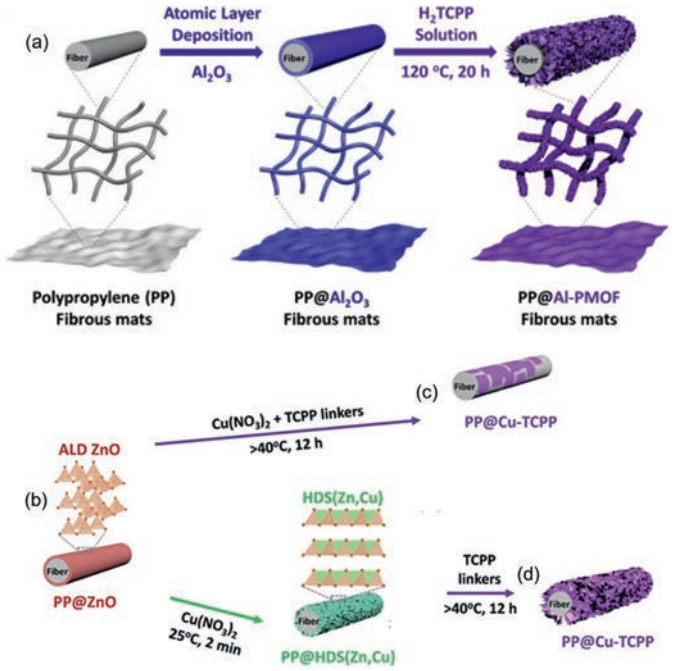

Fig. 3. (a) Preparation of PP@Al-MOF composite *via* metal oxide coordination replication. Reproduced with permission [84]. Copyright 2020, Elsevier. (b) Orientation-controlled preparation of (c) PP@Cu-TCPP (horizontal) and (d) PP@Cu-TCPP (radial). Reproduced with permission [95]. Copyright 2019, Wiley VCH.

form HDS(Zn,Cu) into Cu-TCPP without changing the radial fashion (Fig. 3d). As a universal method, the HDS intermediated method can be also applied in synthesizing PP@M-TCPP composites of other metals (*e.g.*, M = Zn and Co) [95]. In another report, Zhang and co-workers developed a facile method to prepare composite membrane *via* direct growth of 2D MOFs on anodized aluminum oxide (AAO) template. In a typical process, a piece of AAO membrane was added into the solution containing 2-aminoterephthalic acid (H_2BDC-NH_2) and HCl, and the obtained reaction system was then kept in hydrothermal conditions. Al_2O_3 on the surface of AAO membrane was gradually dissolved in the presence of HCl, and the *in situ* generated Al^{3+} was then connected with H_2BDC-NH_2, thereby forming MIL-53-NH_2 nanoplates on the surface of AAO membrane [96].

3. Applications of 2D MOF nanosheet composites

3.1. Gas separation and adsorption

The separation of CO_2 from gaseous mixtures is a key procedure in water-gas shift process [97,98]. In a typical research, the CuBDC-GO hybrid membrane was utilized to separate the gaseous mixture of CO_2 and H_2. Because of the interfacial voids existing in the pure CuBDC membrane or CuBDC-GO hybrid membrane but with a relatively low GO content, CO_2 molecules are likely to leak out and resulted in low H_2/CO_2 separation selectivity (7.3:1). Fortunately, the CuBDC-GO hybrid membrane having optimal GO amount exhibited a H_2/CO_2 selectivity higher than 100:1 since the voids were thoroughly filled by GO. However, excessive GO usually led to poor H_2 permeance due to the rapidly rising mass transfer resistance in resultant composite membrane (Fig. 4) [41].

As a type of toxic and irritating gas, ammonia widely occurred in biochemical processes, and adsorbent of high capacity is desired in NH_3 removal. In a typical work, Cu-TCPP MOF coated PP fiber, PP@Cu-TCPP, has been developed and applied in NH_3 adsorption. Under identical dry conditions, PP@Cu-TCPP exhibited

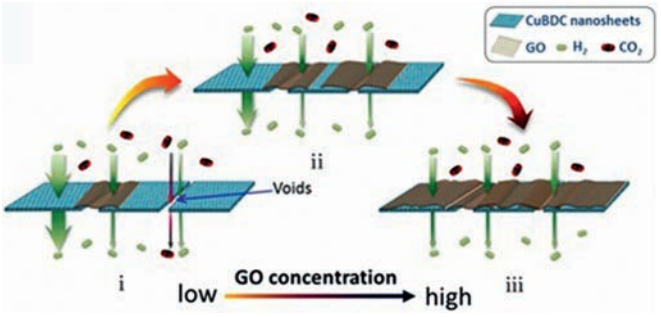

Fig. 4. Schematic view of gas molecule diffusion through CuBDC-GO composite membranes with different GO concentration. Reproduced with permission [41]. Copyright 2018, American Chemical Society.

higher NH_3 adsorption capacity (2.0 mol/kg_{MOF}) in comparison to pure Cu-TCPP powder (1.2 mol/kg_{MOF}). Moreover, the presence of moisture can magnify the advantage of PP@Cu-TCPP composite in further. At a relative humidity of 80%, PP@Cu-TCPP showed a significant improvement on NH_3 adsorption performance (3.5 mol/kg_{MOF}), whereas no enhancement was observed for Cu-TCPP powder. The abundant external surface sites exposed from the radially aligned Cu-TCPP nanosheets onto PP fiber were contribute to the higher adsorption capacity of PP@Cu-TCPP towards incoming polar molecules (*i.e.*, NH_3 and H_2O). Moreover, the higher water adsorption capability of PP@Cu-TCPP can further improve its ammonia uptake thanks to the formation of hydrogen bond between the preformed water film with ammonia [95].

3.2. Energy conversion and storage

A number of MOF nanosheet composites have been applied as active components for energy conversion processes, such as hydrogen evolution reaction (HER) [36,55,69,99], oxygen evolution reaction (OER) [42,99–101], CO_2 reduction reaction (CO_2RR) [85,102] and photoelectrochemical (PEC) cells [82].

In a typical research, Lin and coworkers designed a hybrid material combining 2D Hf_{12}-CoDBP (DBP = 5,15-di(*p*-benzoato)-porphyrin) MOF nanosheets with CNT, in which the carboxylate substitutes on CNT directly bonded to the secondary building blocks (SBUs) of Hf_{12}-CoDBP. First of all, the coordination bond mode between Hf_{12}-CoDBP and CNT endows the composite with superior conductivity, that is, improved electron transfer rate from the electrode surface to the CoDBP catalytic sites. Besides, the sheet-like shape of Hf_{12}-CoDBP renders the CoDBP catalytic site communicating to the electrolyte, substrate and conductive support more efficiently. Moreover, the porous nature of Hf_{12}-CoDBP endows the composite with rich catalytically active sites. In brief, these characters make Hf_{12}-CoDBP/CNT a good HER electrocatalyst. Namely, an onset potential of 315 mV and a turnover frequency (TOF) of 17.7 s^{-1} were obtained in the acidic medium [36].

It has been well accepted that the adsorption energy of H* and OH* (* refers to species bound to the catalyst surface) intermediates can impact the catalytic activity of HER and OER catalyst, respectively [103–105]. Qiao and coworkers reported a hybrid Pt NC/Ni-MOF material, in which Pt NCs were incorporated into 2D MOF nanosheets constructed with nickel(II) and BDC linker (Ni-MOF). As X-ray photoelectron spectroscopy (XPS) revealed, Ni-O-Pt bonds were formed at the interface between Pt NCs and Ni-MOF, which can increase the electron density of Pt NCs and meanwhile reduce the electron density of Ni-MOF. As a result, the adsorption energy of H* onto the Pt NC/Ni-MOF became slightly weaker than free Pt NCs, and the adsorption energy of OH* on the Ni site was strengthened in comparison with pristine Ni-MOF, thus improving the catalytic activity of both HER and OER (Figs. 5a-d). In the al-

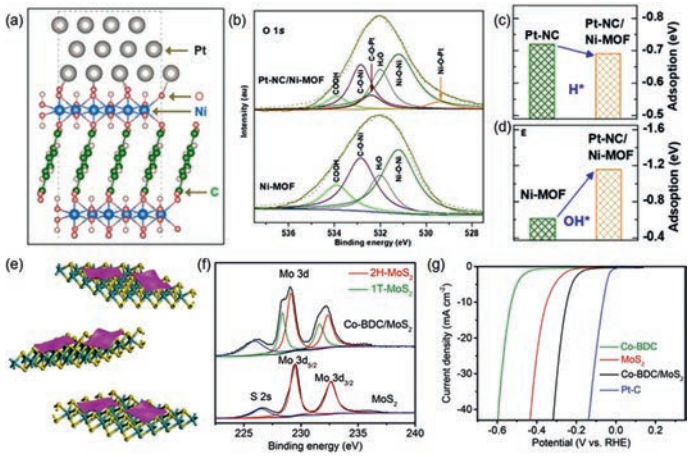

Fig. 5. (a) Structural model of Pt-NC/Ni-MOF. (b) XPS O 1s spectrum, (c) H* adsorption energy and (d) OH* adsorption energy of Ni-MOF and Pt-NC/Ni-MOF. Reproduced with permission [99]. Copyright 2019, Elsevier. (e) Structural model, (f) XPS Mo 3d spectrum and (g) linear sweep voltammetry curve of Co-BDC/MoS_2 in HER. Color of model: purple sheet, Co-BDC; cyan, Mo; yellow S. Reproduced with permission [55]. Copyright 2019, Wiley-VCH.

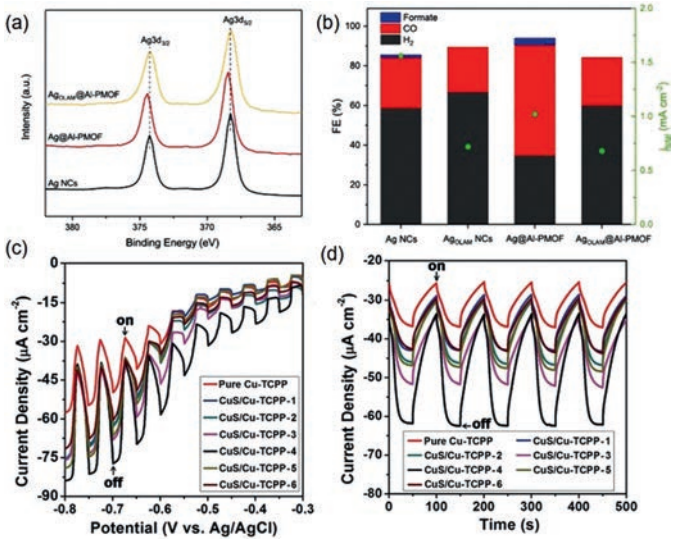

Fig. 6. (a) XPS Ag 3d spectra and (b) Faradic efficiency of Ag NCs, Ag@Al-PMOF and Ag_{OLAM}@Al-PMOF for CO_2RR, wherein Ag_{OLAM} refers to Ag NCs covered with oleylamine, in which the MOF-to-Ag electron transfer is prohibited. Reproduced with permission [102]. Copyright 2019, Wiley-VCH. (c) Linear sweep voltammograms (LSV) curves and (d) transient photocurrent responses at -0.6 V (*vs.* Ag/AgCl) bias potential of Cu-TCPP nanosheets and CuS/Cu-TCPP-n composite nanosheets, wherein n refers to the sulfidation reaction time (hour) during composite preparation. Larger n value leads to higher CuS content. Reproduced with permission [82]. Copyright 2016, Wiley-VCH.

kaline medium, the HER mass activity of Pt-NC/Ni-MOF reached 7.92 mA/μg_{Pt} (at a 70 mV overpotential), over 2.5 times higher than free Pt NCs. Correspondingly, the OER current density reached 39.6 mA/cm^2 (at a 340 mV overpotential), 5.5 times higher than the pristine Ni-MOF [99].

In addition to Pt NCs, transitional metal dichalcogenides (*e.g.*, MoS_2) are considered as an alternative active component in HER due to its low cost, good chemical stability and suitable H* adsorption energy. Generally, MoS_2 exists in several different phases (*e.g.*, 1T, 1H, 2H and 3R), among which the 2H phase is most stable in thermodynamics. However, the electron conductivity of 2H MoS_2 is relatively poor. Besides, only a small portion of sites (*i.e.*, unsaturated edge sites) exposed by the 2H MoS_2 are active in HER. In comparison, 1T MoS_2 possesses higher electron conductivity and larger active site proportion, making it preferable as HER electrocatalysis [106]. Qiao *et al.* developed 2D Co-BDC/MoS_2 hybrid nanosheets by depositing Co-BDC on the surface of the thermodynamically stable 2H MoS_2. The incorporation of Co-BDC is supposed to increase the electron density of MoS_2, and thus leads to a partial phase transformation from 2H to 1T. Moreover, the Co-BDC part can accelerate the water dissociation step efficiently in the alkaline medium. In combination, the precisely designed Co-BDC/MoS_2 hybrid nanosheets exhibited a 10 mA/cm^2 HER current density at an overpotential of 248 mV, which was much lower than that of separate MoS_2 (349 mV) and Co-BDC (529 mV) (Figs. 5e-g) [55].

CO_2RR is of high significance in carbon neutralization [107–109]. The applications of MOF nanosheet composites in electrochemical CO_2RR has been vastly reported as well. For example, Ag@Al-PMOF (PMOF refers to $Al_2(OH)_2$(TCPP)), in which spherical Ag NCs on a conducive substrate were covered with a layer of $Al_2(OH)_2$(TCPP), was applied as a CO_2RR electrocatalyst in $KHCO_3$ aqueous solution. Generally, CO_2RR catalysts are in face of the challenge of HER competition. In this case, Ag and Al-PMOF are in close contact with each other in order to increase the electron density of catalytic Ag NCs (as confirmed by XPS) *via* electron transfer from Al-PMOF, thus facilitating the reduction ability of Ag NCs towards CO_2. As a result, in comparison to pure Ag NCs, Ag@Al-PMOF exhibited a higher CO_2RR activity with producing formate and carbon monoxide (Figs. 6a and b) [102]. In another work, ZnO decorated $Al_2(OH)_2$(TCPP) MOF prepared *via* the VPI method was applied in electrochemical CO_2RR. As mentioned in Section 2.1 (Fig. 1d), the growth of ZnO can induce internal strain inside MOF structure, and therefore partially deform the coordination sphere of the catalytic Zn site at the center of porphyrin ring for CO_2RR activity improvement. As expected, at an overpotential of −1.2 V, the ZnO decorated $Al_2(OH)_2$(TCPP) exhibited much higher Faradic efficiency (FE) (33%) than the Zn ion-metalated $Al_2(OH)_2$(TCPP) (8%) [85].

The composites constructed from MOF nanosheets have been also applied in PEC cells. For instance, TCPP-based MOF nanosheets possess high visible light absorption ability and good stability against photobleaching, making them as promising candidates for PEC. Nevertheless, their performance is still limited by the fast recombination of excitons. In order to facilitate the separation of excitons, a feasible strategy is to construct heterojunctions by combining TCPP-based MOF nanosheets with semiconductor NPs. For example, our group investigated the PEC performance of CuS/Cu-TCPP, in which CuS NPs were decorated on the surface of 2D Cu-TCPP nanosheets (as previously illustrated in Figs. 1a-c). In a typical experiment, fluorine-doped tin oxide (FTO) glass coated with primary Cu-TCPP or CuS/Cu-TCPP composite film was tested as the photoelectrode. One can clearly see that much improved photocurrent density was obtained upon using the CuS/Cu-TCPP composite with optimal CuS amount (Figs. 6c and d), in comparison to pure Cu-TCPP. This is because that, on one hand, the type-II heterojunction formed between CuS and Cu-TCPP can enhance the separation of photo-generated carriers; on the other hand, the higher charge mobility of CuS is conducive to the charge transfer between the active material layer and the electrode [82].

In addition, a type of nano-composite combining Cu-TCPP MOF and PPy polymer, Cu-TCPP@PPy, has been prepared and applied as the electrochemical capacitor. In comparison with pure PPy, the Cu-TCPP@PPy composite possesses increased electrochemically active surface area and decreased ion diffusion length, which together lead to higher charge transfer efficiency. Moreover, when compared with pristine Cu-TCPP, the PPy coating endows the composite with improved electron transport capability due to the good conductive nature of PPy and the strong π-π interaction between

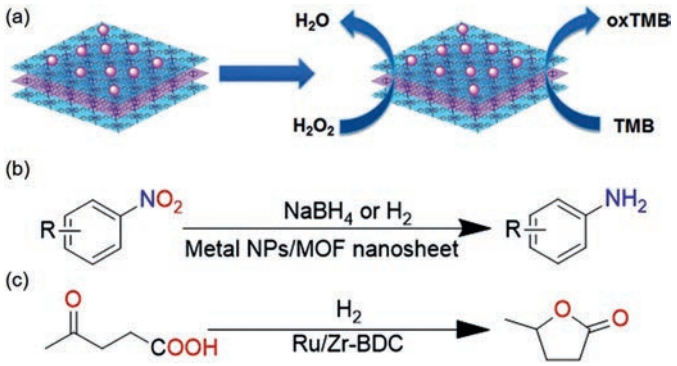

Fig. 7. (a) Cascade reactions catalyzed by Au NPs/Cu-TCPP(M) composites. Reproduced with permission [66]. Copyright 2017, Wiley-VCH. (b) Reduction of nitroarene on MOF nanosheet composites. (c) Hydrogenation cyclization of levulinic acid on Ru/Zr-BDC composite nanosheets.

PPy and Cu-TCPP. Impressively, a maximal specific capacitance of 496 F/g was achieved at 1 A/g current density for Cu-TCPP@PPy, which was significantly higher than pure PPy (245 F/g), Cu-TCPP (negligible) and their simple mechanical mixture (176 F/g). In addition, the close contact between Cu-TCPP and PPy at the interface can efficiently buffer the volume change during charging and discharging process, thereby ensuring the excellent cycling stability of the composite electrode (*i.e.*, at a high current density of 20 A/g, nearly 70% of the initial capacitance could be kept after 3000 circles) [43].

3.3. Catalysis

The large planar dimension and ultrathin thickness donate ultrahigh external surface area to MOF nanosheet composites, which are expected to serve as the ideal support used for heterogeneous catalysts. Lots of researches have explored the catalytic applications of metal NPs-incorporated MOF nanosheets [75,110]. For example, our group employed Cu-TCPP(M) (TCPP = tetrakis(4-carboxyphenyl)porphyrin; M = Fe, Co) nanosheets as the support for growing gold NPs. Since Au NPs can function as glucose oxidase analogue, and meanwhile 2D metalloporphyrinic MOFs are able to exhibit peroxidase-like catalytic activity, as-resultant Au NPs/Cu-TCPP(M) composite was used as the biomimicking catalyst for cascade reactions. First, with the existence of oxygen, Au NPs/Cu-TCPP(M) promoted the conversion of glucose to gluconic acid, which was accompanied with the generation of H_2O_2. Simultaneously, 3,3′,5,5′-tetramethylbenzidine (TMB) was transformed into oxidized 3,3′,5,5′-tetramethylbenzidine (oxTMB) by the *in-situ* formed H_2O_2 (Fig. 7a). According to results of control experiments, no conversion of TMB was observed without the presence of either glucose or Au NPs/Cu-TCPP(M), proving that the dual function of Au NPs/Cu-TCPP(M) composites are essential to catalyze the cascade reaction [66].

Lu and coworkers incorporated ultrasmall Au NPs into a type of nickel MOF nanosheet, [NMOF-Ni, Ni_2(5,4-PMIA)$_2$(TPOM)$_{0.5}]_n$ (5,4-PMIA = 5-(4-pyridyl)-methoxylisophthalic acid; TPOM = tetrakis(4-pyridyloxymethylene)methane), and the obtained Au-1@NMOF-Ni composite was utilized to catalyze the reduction of nitro compounds (*e.g.*, 4-nitrophenol) with $NaBH_4$ (Fig. 7b). Because of the confinement of NMOF-Ni, no obvious aggregation of Au NPs occurred during the catalyst preparation as well as performance test. Consequently, Au-1@NMOF-Ni showed much higher catalytic activity (100% conversion was reached after reaction of 6 min) and better reuse performance (no obvious activity loss after ten consecutive catalytic cycles) than isolated Au NPs (100% conversion was achieved after reaction of 20 min, but the conversion rate was dropped to 20% after ten consecutive catalytic cycles) [111]. In another work, a type of copper-based 2D MOF nanosheet, Cu(HBTC)$(H_2O)_3$ (namely, Cu(HBTC)-1), was applied as the supporter to load Ag, Au, Pd, Pt NPs or their alloys. The 4-nitrophenol reduction with $NaBH_4$ was also chosen as the model reaction to evaluate the catalytic performance of prepared metal NPs/Cu(HBTC)-1 composites. Among which, the ternary and binary alloy composites (*e.g.*, $Au_{0.3}Pt_{0.3}Pd_{0.4}$/Cu(HBTC)-1, $Au_{0.4}Pd_{0.6}$/Cu(HBTC)-1 and $Au_{0.4}Pt_{0.6}$/Cu(HBTC)-1) gave higher catalytic rate constants (0.31-0.48 min^{-1}) than the monometallic ones (*e.g.*, Pd/Cu(HBTC)-1, Au/Cu(HBTC)-1, Pt/Cu(HBTC)-1 and Ag/Cu(HBTC)-1) (0.17-0.27 min^{-1}), possibly attributed to the synergic effect among multiple metal species [67].

Hydrogenation reactions catalyzed by 2D MOF nanosheet composites have been widely investigated as well. Wang *et al.* immobilized Pd NPs onto the hierarchical-pore 2D nanosheets of MOF-5 (donated as H-MOF-5). The resultant Pd-H-MOF-5 composite was used to promote the hydrogenation of nitroarene. Thanks to the existence of abundant mesopores, Pd-H-MOF-5 was more efficient in the catalytic hydrogenation compared with bulk MOF-5 supported Pd NPs (Pd@bulk MOF-5). Namely, under identical reaction conditions (H_2 1 atm, 60 °C, 1.5 h), Pd-H-MOF-5 gave near 100% conversion of nitrobenzene, much higher than the ~40% achieved by Pd@bulk MOF-5 [71]. More significantly, the hydrogenation of levulinic acid (LA) to yield cyclic γ-valerolactone (GVL) is a key process in the chemical transformation of biomass (Fig. 7c). Ru NPs deposited 2D-UiO-66 nanosheets (Ru/2D-UiO-66) was employed in the catalysis of the LA-to-GVL conversion. The reaction could proceed under 3 MPa H_2 at 90 °C, and the TOF of Ru/2D-UiO-66 composite nanosheets (349 h^{-1}) was nearly 10 times as high as that of Ru NPs deposited bulk 3D-UiO-66 crystals (38.1 h^{-1}). The highly exposed catalytic sites and reduced geometric restraints of 2D-UiO-66 nanosheets were considered as main contributions for the superior performance [72].

In addition to metal NPs, single-metal site incorporated 2D MOFs have also been substantially applied in the field of heterogeneous catalysis. For instance, Wang and coworkers reported Cu(I) modified Zr_{12}-BPDC 2D MOF (as mentioned in Section 2.1) for CO_2 reduction by hydrogen. In resultant Zr_{12}-BPDC-CuCs composite, the negatively charged Zr_{12} cluster $[Zr_{12}O_8(\mu_3\text{-}O^-)_8(\mu_2\text{-}O^-)_6(COO^-)_{18}]^{14-}$ is balanced with eleven Cu(I) and three Cs^+. Impressively, the closely spaced Cu(I) sites anchored on the same Zr_{12} node can form Cu(I)-Cu(I) bimetallic active site for boosting carbon-carbon coupling product (*e.g.*, ethanol). In contrast with zirconia supported Cu NPs, which gave methanol as the main hydrogenation product, Zr_{12}-BPDC-CuCs exhibited a turnover number (TON) up to 4080 toward ethanol product [77].

A MOF-on-MOF composite, PCN-222(Co)@MTTB (MTTB refers to a metal-organic layer constructed with the classical Zr_6 cluster and 4,4′,4″-*s*-triazine-2,4,6-triyl-tribenzoate, TTB), was developed recently as the efficient catalyst for CO_2 cycloaddition of epoxides (Fig. 8a). In which, the surface of PCN-222(Co) nanosticks is covered with MTTB nanosheets. It is worthy to mention that the abundance of Lewis acidic (Co and Zr) and alkaline (TTB) sites are both favored in the CO_2 cycloaddition of epoxides. Taking butyl glycidyl ether as the representation, as-obtained composite gave 52% yield of corresponding cyclic carbonate product under 50 °C and 1 atm CO_2. It was higher than separate PCN-222(Co) (32%) and MTTB (36%) as well as their simple mixture (34%), implying a synergic effect between the two MOF components [44].

Since porphyrin species are active in the generation of singlet oxygen ($^1O_2$) under the irradiation of visible light, the PP@Al-PMOF composite (Fig. 3a) can be applied in the photocatalytic oxidation of 2-chloroethyl ethyl sulfide (CEES), a simulant of sulfur mustard blistering agent, into non-toxic 2-chloroethyl ethyl sulfoxide (Fig. 8b). In the presence of oxygen and under the irradiation

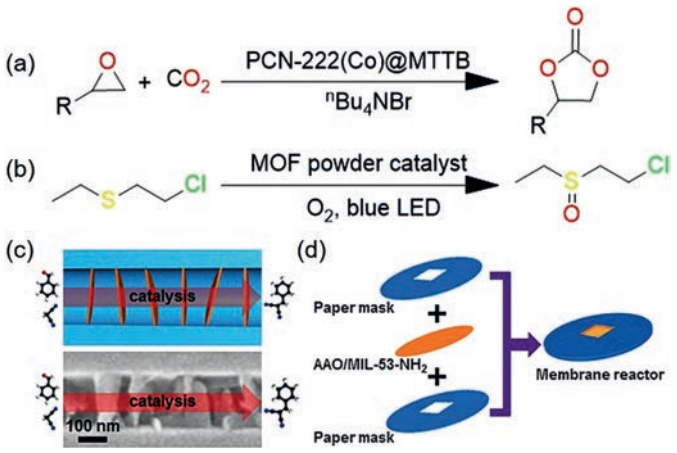

Fig. 8. (a) CO_2 cycloaddition catalyzed by PCN-222(Co)@MTTB. (b) Photocatalytic oxidation of CEES catalyzed by PP@Al-PMOF. (c) AAO/MIL-53-NH_2 composite and (d) membrane reactor for Knoevenagel reaction between benzaldehyde and malononitrile. Reproduced with permission [96]. Copyright 2017, Wiley-VCH.

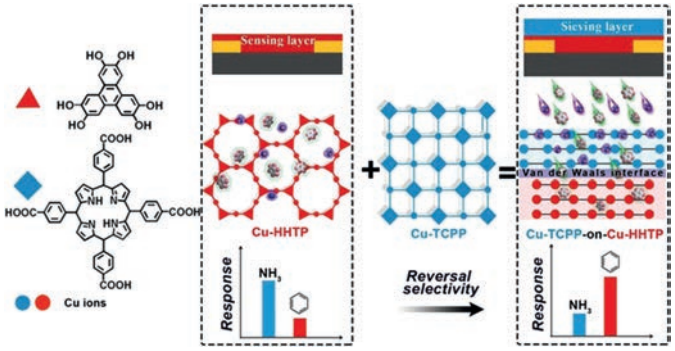

Fig. 9. Cu-TCPP-on-Cu-HHTP composite film for highly selective sensing of benzene. Reproduced with permission [91]. Copyright 2019, Wiley-VCH.

of blue LED illuminant, PP@Al-PMOF led to a TOF of 170 mol_{CEES} $mol_{chromophore}^{-1}$ min^{-1}, nearly 20 times of the separate Al-PMOF powder (9 mol_{CEES} $mol_{chromophore}^{-1}$ min^{-1}). Reasoningly, the MOF nanosheets bound to the surface of the textile PP substrate can be prevented from aggregation for absorbing light illumination more efficiently, which may account for the significant enhancement in the photocatalytic efficiency [84].

Although heterogeneous catalysts can be recollected after reaction, in many cases, they are dispersed in the catalytic system, and an additional separation step, such as filtration and centrifugation, is still needed. The applications of MOF-based composite membranes can avoid the extra separation operation. For instance, 2D anodized aluminum oxide (AAO)/MOF composite was developed as the membrane reactor to catalyze the Knoevenagel condensation. First, MIL-53-NH_2 nanosheets featured with catalytically active amino groups grew in the channels of AAO membrane to form AAO/MIL-53-NH_2. The resultant composite was then installed in a dead-end membrane module to construct a type of membrane reactor for the Knoevenagel reaction of benzaldehyde and malononitrile (Figs. 8c and d). The AAO/MIL-53-NH_2-based membrane reactor showed a benzylidenemalononitrile yield of about 50% at the beginning of reaction and the yield could be kept almost unchanged for 60 min, which was higher in stability than the batch reaction system using bulk MIL-53-NH_2 powder. In addition, no significant loss of activity was observed for AAO/MIL-53-NH_2 after three consecutive catalytic cycles [96].

3.4. Sensing

By virtue of the abundantly exposed active sites, MOF nanosheet composites are promising candidates for sensing applications. Our group has developed Au NPs/Cu-TCPP(Fe) hybrid nanosheets, which can be applied in the detection of glucose. In the colorimetric experiment, with the concentration of glucose increasing, the absorbance peak centered at 652 nm (attributed to oxTMB) increased linearly. The glucose limit-of-detection (LOD) of Au NPs/Cu-TCPP(Fe) was as low as 8.5 μmol/L [66]. Another research developed the Au nanowire (NW) decorated Zn-OAM nanobelt (Zn-OAM/Au NW) as well as its derived ZIF-8/Au NW in the applications of electrochemical NO_2 sensing. With the concentration of NO_2 increasing, both composites display rapid resistance declining (response time < 10 s) thanks to the incorporation of Au nanowires of good conductivity. More impressively, ZIF-8/Au NW is even better in sensitivity (LOD = 190 ppb) than Zn-OAM/Au NW (LOD = 760 ppb) [112].

A heterostructural Cu-TCPP-on-Cu-HHTP (as illustrated previously in Section 2.1) composite was developed for the selective sensing of benzene. Normally, the pure Cu-HHTP exhibits a high chemiresistive response toward benzene but suffers from low detection selectivity caused by the interference of other molecules (*e.g.*, ammonia). In the Cu-TCPP-on-Cu-HHTP composite, the Cu-TCPP sieving layer above Cu-HHTP can preferably capture the ammonia molecule, as its coordinatively unsaturated Cu site has a stronger affinity toward ammonia than benzene. As expected, the sensing selectivity (*i.e.*, the chemiresistive response ratio between benzene and ammonia) of Cu-TCPP-on-Cu-HHTP composite film was improved by more than 250% in comparison to pure Cu-HHTP (Fig. 9) [91].

2D MOF nanosheet composites also show great application prospects in biosensing [113,114]. For example, an oligonucleotide modified metal cluster-MOF nanosheet composite, Apt/AuNCs@521-MOF (521-MOF = $Zr_6(\mu_3\text{-}O)_8(NBB)_{0.67}(CF_3COO)_6$, NBB = 4′,4″,4‴′-nitrilotris((1,1′-biphenyl)-4-carboxylate), Apt = cocaine aptamer), was developed for the electrochemical sensing of cocaine. The high affinity of Zr center of Apt/AuNCs@521-MOF toward the phosphate group of cocaine allows firm immobilization of cocaine aptamer for acquiring excellent selectivity. Deservedly, Apt/AuNCs@521-MOF has exhibited a low LOD of 1.29 pmol/L and a wide linear detection range of 0.001-1.0 ng/mL [115]. In another work, G-quadruplex-hemin (G4-hemin) decorated 2D Cu-TCPP MOF was employed as a type of electrochemical sensor for hydrogen peroxide. The porous nature and 2D morphology of Cu-TCPP offered high density of H_2O_2-interactive sites. Meanwhile, G4-hemin, as a DNAzyme *via* combination of G-quadruplex DNA and hemin, possesses peroxidase-like bioactivity. The Cu-TCPP/G4-hemin-based electrochemical sensor exerted low LOD (0.03 μmol/L) and high sensitivity (> 2000 μA L cm^{-2} $mmol^{-1}$), as well as excellent anti-interference capability against major interfering substances such as ascorbic acid, acetaminophen, glucose and uric acid [92].

3.5. Biomedicine

Antibacterial agents with high efficiency and low toxicity are of great significance in clinic applications [116]. As a strong oxidant, hydroxy radial (•OH) may function as a type of powerful specie for disinfection [117]. A key route to generate •OH is the homolysis of H_2O_2 in the presence of peroxidase (POD) or its analogues. Au NPs exhibit intrinsic POD mimicking activity, and hence, can be combined with MOF supports for antibacterial usage. For example, a nano-composite composed of ultrasmall Au NPs and 2D Al-TCPP MOF (denoted as UsAuNPs/MOFs) was developed for antibacterial

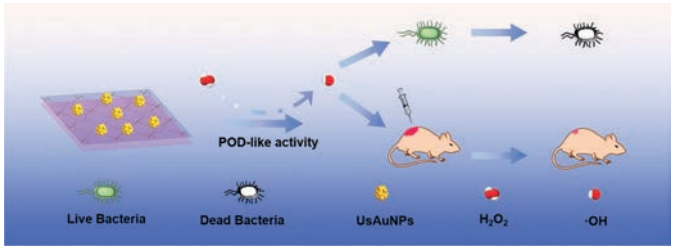

Fig. 10. *In vitro* and *in vivo* antibacterial applications of 2D UsAuNPs/MOFs nanosheet composite. Reproduced with permission [118]. Copyright 2020, Wiley-VCH.

therapy. The installation of UsAuNPs on 2D MOF may prevent the particle aggregation, thereby allowing a higher density of exposed catalytically active sites compared with unsupported Au NPs. Besides, the diffusion resistance of 2D MOF is quite low thanks to its ultrathin thickness. In the *in vitro* antibacterial tests against *Staphylococcus aureus* and *Escherichia coli* with a small amount of H_2O_2, UsAuNPs/MOFs showed superior performance (bacterial viability $< 20\%$) in comparison to separate Al-TCPP (bacterial viability $> 80\%$). In addition, the mouse experiment revealed that the composite exhibited good biocompatibility as well as efficient *in vivo* wound healing performance (Fig. 10) [118]. Another research reported 2D Cu-TCPP(Fe) MOF nanosheets as the supporter for glucose oxidase immobilization. Since glucose oxidase can catalyze the oxidation of glucose accompanied with the generation of H_2O_2, and meanwhile Cu-TCPP(Fe) is capable of homolysis of H_2O_2 into $^{\bullet}OH$ radial, the composite is competent in the antibacterial applications without extra addition of H_2O_2; hence, the potential risk of side effects on health can be reduced [40].

As a novel non-invasive therapeutic strategy, photodynamic therapy (PDT) has displayed a grand prospect in oncotherapy [119–121]. Generally, the efficiency of PDT is highly related to the intrinsic characteristics of photosensitizer (PS). Unfortunately, the aggregation, photobleaching and poor solubility of conventional organic PS may impair the PDT performance [122]. At this point, 2D MOF-based PS may circumvent such issues. Besides, the less mass transfer restriction of 2D MOF nanosheets compared with their 3D bulk counterparts is conducive to further enhancement of PDT effect. In a typical research, Sm-TCPP nanosheets decorated with Pt NPs were developed for PDT. First of all, Sm-TCPP possesses a high capability for reactive oxygen species (ROS) generation due to the high installation amount of TCPP linker functioning as PS. Besides, Pt NPs uniformly dispersed on Sm-TCPP nanosheets can mimic the performance of catalase, which facilitates the conversion of overexpressed H_2O_2 into O_2 in tumor microenvironment. As-generated O_2 can be further converted to highly active singlet oxygen ($^1O_2$) over Sm-TCPP under visible light irradiation. Therefore, the synergistic effect between Sm-TCPP and Pt NPs endows the Sm-TCPP-Pt composite with high PDT performance. Furthermore, in order to improve the target ability toward tumor cells, triphenylphosphine (TPP), a mitochondrion-targeting molecule, was further integrated into Sm-TCPP-Pt. In the *in vitro* experiment, as expected, most of the Sm-TCPP-Pt/TPP nanosheets were gathered around or inside mitochondria. Moreover, *in vivo* tests based on the MCF-7 murine models with pristine tumor volumes of 200 mm^3 confirmed the validity of the composites. That is, after a 15-day treatment, the tumor volumes in mice treated with pure Sm-TCPP, Sm-TCPP-Pt and Sm-TCPP-Pt/TPP were 500, 300 and 100 mm^3, respectively [123].

3.6. Other applications

MOF nanosheets and their composites containing Brønsted acid moieties have also been widely used as proton-conductors [124,125]. For example, a DNA@ZIF-8/AAO composite membrane was developed, in which the ZIF-8 layer with single-strand DNA molecules threading through was coated onto the AAO substrate. When employed as the proton exchange membrane in methanol fuel cells, the DNA@ZIF-8/AAO composite membrane exhibited quite low permeability of methanol (1.25×10^{-8} cm^2/s) thanks to the small pore size of ZIF-8 and the high integrity of the resultant composite membrane. In addition, a high proton conductivity (3.40×10^{-4} S/cm at 25 °C and 0.17 S/cm at 75 °C) was obtained for the DNA@ZIF-8/AAO composite membrane under humid conditions, attributed to the hydrogen bonding between water molecules inside ZIF-8 channels and amidogen/phosphate groups of DNA molecules [126].

MOF nanosheet composites are also promising in the applications of luminescence [127,128]. For example, some MOF materials possess thermochromic characteristics; but it is challenging to use them to fabricate imaging devices due to their poor intrinsic mechanical strength. This problem can be solved by integrating MOF nanosheets with flexible materials. In a typical work, two types of thermochromic MOF nanosheets, CuCT and CuMCT (CT = 4-carboxythiophenolate; MCT = 4-methoxycarbonylthiophenolate), were integrated with polyvinylidene difluoride (PVDF) thin films, respectively. The as-resultant composites inherited the thermochromisms of their constituent MOF nanosheets. That is, CuCT@PVDF presented a thermochromic behavior under ultraviolet irradiation, with its color changing from pale yellow (300 K) to green (200 K) and orange (77 K), and CuMCT@PVDF exhibited a color variation from pale orange (300 K) to green (77 K). Furthermore, CuCT@PVDF and CuMCT@PVDF possessed minimal macroscopic defects and high mechanical strength, making them potential candidates for 2D imaging films [127].

4. Conclusion and perspectives

2D MOF nanosheets possess many appealing characteristics, such as large surface area, good machinability, high accessibility of active sites, small mass transfer resistance, tunable structure and morphology as well as facile functionalization ability. Further combination of MOF nanosheets with other materials to assemble composites can not only combine the chemical and physical properties (*e.g.*, stability, compactness, flatness, mechanical strength, light absorbance and electrical conductivity) of the pristine component, but also introduce exceptional functionalities stemming from the synergistic effect, thus widely expanding the application scope and obviously enhancing the performance of the resultant MOF nanosheet composites.

In general, two types of methods have been developed to combine MOF nanosheets with other materials: (1) MOF nanosheets act as supporters for growth of other materials; (2) growth of MOF nanosheets on other materials. To date, a number of materials, such as metal nanoparticles, single-metal sites, metal oxides, metal sulfides, graphene, CNT, polymers, biomacromolecules and even other type of MOFs, have been integrated with MOF nanosheets. These composites have exhibited promising prospects in various usages, such as gas separation and adsorption, energy conversion and storage, heterogeneous catalysis, sensing and biomedicine.

Despite much progress having been made, further researches are still required in this hot research field. First of all, MOF nanosheet composites with high stability are urgently desired, especially under harsh chemical/electrochemical conditions, *e.g.*, highly acidic or alkaline solution. This may broaden the application scope of MOF nanosheet composites in practice. Besides, more efficient strategies to integrate MOF nanosheets with other components, for instance, eliminating the crystalline and porosity loss of MOFs during composite preparation as well as developing composites with more exquisite structure and morphology, need to be

further explored. Last but not least, the interaction between MOF nanosheet composites and objective substances (*e.g.*, feeds in gas separation, substrates/products in chemical reactions and analytes in sensing) in particular applications needs to be investigated in-depth. This will be instructive for the rational design of composites of high performance as a return.

Declaration of competing interest

The authors declare no competing financial interests or associative interest in connection with the work submitted.

Acknowledgments

This work is supported by National Natural Science Foundation of China (No. 21905195), Natural Science Foundation of Tianjin City (No. 20JCYBJC00800) and PEIYANG Young Scholars Program of Tianjin University (No. 2020XRX-0023).

References

[1] X. Huang, X. Qi, F. Boey, et al., Chem. Soc. Rev. 41 (2012) 666–686.
[2] H. Zhang, Chem. Rev. 118 (2018) 6089–6090.
[3] Z. Dai, L. Liu, Z. Zhang, Adv. Mater. 31 (2019) 1805417.
[4] F. Xia, H. Wang, D. Xiao, et al., Nat. Photonics 8 (2014) 899–907.
[5] C. Tan, H. Zhang, Chem. Soc. Rev. 44 (2015) 2713–2731.
[6] Y.L. Huang, W. Chen, A.T.S. Wee, SmartMat 2 (2021) 139-153.
[7] M. Chhowalla, Z. Liu, H. Zhang, Chem. Soc. Rev. 44 (2015) 2584–2586.
[8] M. Chhowalla, H.S. Shin, G. Eda, et al., Nat. Chem. 5 (2013) 263–275.
[9] H. Yin, Z. Tang, Chem. Soc. Rev. 45 (2016) 4873–4891.
[10] M. Sun, C. Zhang, D. Chen, et al., SmartMat 2 (2021) 213–225.
[11] P. Flouda, S.A. Shah, D.C. Lagoudas, et al., Matter 1 (2019) 1532–1546.
[12] L. Kong, C. Tang, H.J. Peng, et al., SmartMat 1 (2020) e1007.
[13] H. Li, Z. Song, X. Zhang, et al., Science 342 (2013) 95–98.
[14] G. Liu, W. Jin, N. Xu, Angew. Chem. Int. Ed. 55 (2016) 13384–13397.
[15] H.C. Zhou, J.R. Long, O.M. Yaghi, Chem. Rev. 112 (2012) 673–674.
[16] H. Furukawa, K.E. Cordova, M. O'Keeffe, et al., Science 341 (2013) 1230444.
[17] T. Xia, Y. Lin, W. Li, et al., Chin. Chem. Lett. 32 (2021) 2975–2984.
[18] L. Chen, Q. Xu, Matter 1 (2019) 57-89.
[19] J. Guo, Y. Qin, Y. Zhu, et al., Chem. Soc. Rev. 50 (2021) 5366–5396.
[20] L. Cao, C. Wang, ACS Cent. Sci. 6 (2020) 2149–2158.
[21] J.X. Wu, W.W. Yuan, M. Xu, et al., Chem. Commun. 55 (2019) 11634–11637.
[22] Y. Wang, M. Zhao, J. Ping, et al., Adv. Mater. 28 (2016) 4149–4155.
[23] M. Zhao, Y. Wang, Q. Ma, et al., Adv. Mater. 27 (2015) 7372–7378.
[24] J. Guo, Y. Zhang, Y. Zhu, et al., Angew. Chem. Int. Ed. 57 (2018) 6873–6877.
[25] Y.H. Xiao, Z.G. Gu, J. Zhang, Nanoscale 12 (2020) 12712–12730.
[26] Z. Zhang, Acta Phys. Chim. Sin. 37 (2021) 2010025.
[27] S.R. Vaddipalli, S.R. Sanivarapu, S. Vengatesan, et al., ACS Appl. Mater. Interfaces 8 (2016) 23049–23059.
[28] S. Xue, H. Jiang, Z. Zhong, et al., Microporous Mesoporous Mater. 221 (2016) 220–227.
[29] Z. Deng, H. Yu, L. Wang, et al., J. Mater. Chem. A 7 (2019) 15975–15980.
[30] Y. Jiang, W. Ma, Y. Qiao, et al., Angew. Chem. Int. Ed. 59 (2020) 12795–12799.
[31] B. Tan, H. Zhao, W. Wu, et al., Nanoscale 9 (2017) 18699–18710.
[32] K. Jayaramulu, V.M. Suresh, T.K. Maji, Dalton Trans. 44 (2015) 83–86.
[33] A. Hu, Q. Pang, C. Tang, et al., J. Am. Chem. Soc. 141 (2019) 11322–11327.
[34] K. Jayaramulu, D.P. Dubal, A. Schneemann, et al., Adv. Funct. Mater. 29 (2019) 1902539.
[35] L. Yang, L. Cao, R. Huang, et al., ACS Appl. Mater. Interfaces 10 (2018) 36290–36296.
[36] D. Micheroni, G. Lan, W. Lin, J. Am. Chem. Soc. 140 (2018) 15591–15595.
[37] S. Wan, J. Wu, D. Wang, et al., Chin. Chem. Lett. 32 (2021) 816–821.
[38] Y. Liu, L. Liu, X. Chen, et al., J. Am. Chem. Soc. 143 (2021) 3509–3518.
[39] Y. Song, R. Fan, P. Wang, et al., J. Mater. Chem. C 3 (2015) 6249–6259.
[40] X. Liu, Z. Yan, Y. Zhang, et al., ACS Nano 13 (2019) 5222–5230.
[41] F. Yang, M. Wu, Y. Wang, et al., ACS Appl. Mater. Interfaces 11 (2019) 990–997.
[42] L. Zhao, B. Dong, S. Li, et al., ACS Nano 11 (2017) 5800–5807.
[43] H. Yao, F. Zhang, G. Zhang, et al., Chem. Eng. J. 334 (2018) 2547–2557.
[44] E. Liu, J. Zhu, W. Yang, et al., ACS Appl. Nano Mater. 3 (2020) 3578–3584.
[45] Q. Zhang, P.-S. Cao, Y. Cheng, et al., Adv. Funct. Mater. 30 (2020) 2004854.
[46] Y. Sakata, S. Furukawa, M. Kondo, et al., Science 339 (2013) 193–196.
[47] B. Hu, P. Wu, Nano Res. 13 (2020) 868–874.
[48] X. Huang, P. Sheng, Z. Tu, et al., Nat. Commun. 6 (2015) 7408.
[49] N. Lahiri, N. Lotfizadeh, R. Tsuchikawa, et al., J. Am. Chem. Soc. 139 (2017) 19–22.
[50] D. Zhu, C. Guo, J. Liu, et al., Chem. Commun. 53 (2017) 10906–10909.
[51] T. Rodenas, I. Luz, G. Prieto, et al., Nat. Mater. 14 (2015) 48–55.
[52] M.J. Cliffe, E. Castillo-Martínez, Y. Wu, et al., J. Am. Chem. Soc. 139 (2017) 5397–5404.
[53] P. Chandrasekhar, A. Mukhopadhyay, G. Savitha, et al., J. Mater. Chem. A 5 (2017) 5402–5412.
[54] Y. Ding, Y.P. Chen, X. Zhang, et al., J. Am. Chem. Soc. 139 (2017) 9136–9139.
[55] D. Zhu, J. Liu, Y. Zhao, et al., Small 15 (2019) 1805511.
[56] L. Li, J.D. Yi, Z.B. Fang, et al., Chem. Mater. 31 (2019) 7584–7589.
[57] M. Zhao, Y. Huang, Y. Peng, et al., Chem. Soc. Rev. 47 (2018) 6267–6295.
[58] C. Cui, G. Li, Z. Tang, Chin. Chem. Lett. 32 (2021) 3307–3321.
[59] Y. Xue, G. Zhao, R. Yang, et al., Nanoscale 13 (2021) 3911–3936.
[60] L.P. Tang, S. Yang, D. Liu, et al., J. Mater. Chem. A 8 (2020) 14356–14383.
[61] Y. Wan, M. Song, M. Zhao, Chem. J. Chinese Univ. 42 (2021) 575–594.
[62] G. Li, S. Zhao, Y. Zhang, et al., Adv. Mater. 30 (2018) e1800702.
[63] H. Guo, B. Wang, P. Qiu, et al., ACS Sustain. Chem. Eng. 7 (2019) 8876–8884.
[64] Z. Ma, H. Tian, G. Meng, et al., Sci. China Mater. 63 (2020) 2517–2529.
[65] J. Li, B. Wang, Y. Qin, et al., Catal. Sci. Technol. 9 (2019) 3726–3734.
[66] Y. Huang, M. Zhao, S. Han, et al., Adv. Mater. (2017) 29.
[67] G. Zhan, H.C. Zeng, Adv. Funct. Mater. 26 (2016) 3268–3281.
[68] Q. Qiu, H. Chen, S. Sharif, et al., 2D Mater. 6 (2019) 035008.
[69] K. Rui, G. Zhao, M. Lao, et al., Nano Lett. 19 (2019) 8447–8453.
[70] K. Jayaramulu, K.K.R. Datta, M.V. Suresh, et al., ChemPlusChem 77 (2012) 743–747.
[71] S. He, Y. Chen, Z. Zhang, et al., Chem. Sci. 7 (2016) 7101–7105.
[72] X. Zhang, P. Zhang, C. Chen, et al., Green Chem. 21 (2019) 54–58.
[73] Y. Lin, M. Zhang, L. Zhao, et al., Appl. Surf. Sci. 536 (2021) 147952.
[74] Q. Jiang, J. Xu, Z. Li, et al., Adv. Mater. Interfaces 8 (2021) 2002034.
[75] J. Guo, Y. Wan, Y. Zhu, et al., Nano Res. 14 (2021) 2037–2053.
[76] W. Shi, L. Zeng, L. Cao, et al., Nano Res. 14 (2020) 473–478.
[77] B. An, Z. Li, Y. Song, et al., Nat. Catal. 2 (2019) 709–717.
[78] M. Zhu, Q. Ma, S.Y. Ding, et al., Mater. Lett. 239 (2019) 155–158.
[79] X.Q. Wu, D.D. Huang, Y.P. Wu, et al., ACS Appl. Energy Mater. 2 (2019) 5698–5706.
[80] Y.D. Zhu, Y. Kang, Z.G. Gu, et al., Adv. Opt. Mater. 9 (2021) 2002072.
[81] F. Cao, M. Zhao, Y. Yu, et al., J. Am. Chem. Soc. 138 (2016) 6924–6927.
[82] Q. Lu, M. Zhao, J. Chen, et al., Small 12 (2016) 4669–4674.
[83] C.Z. Leng, M.D. Losego, Mater. Horiz. 4 (2017) 747–771.
[84] D.T. Lee, J.D. Jamir, G.W. Peterson, et al., Matter 2 (2020) 404–415.
[85] F. Yang, W. Hu, C. Yang, et al., Angew. Chem. Int. Ed. 59 (2020) 4572–4580.
[86] Y. Li, L. Lin, M. Tu, et al., Nano Res. 11 (2018) 1850–1860.
[87] Y. Peng, Y. Li, Y. Ban, et al., Science 346 (2014) 1356–1359.
[88] H.T. Kwon, H.K. Jeong, A.S. Lee, et al., J. Am. Chem. Soc. 137 (2015) 12304–12311.
[89] Y. He, Y. Qiao, Z. Chang, et al., Energy Environ. Sci. 12 (2019) 2327–2344.
[90] M. Zhao, J. Chen, B. Chen, et al., J. Am. Chem. Soc. 142 (2020) 8953–8961.
[91] M.S. Yao, J.W. Xiu, Q.Q. Huang, et al., Angew. Chem. Int. Ed. 58 (2019) 14915–14919.
[92] J. Ma, G. Chen, W. Bai, et al., ACS Appl. Mater. Interfaces 12 (2020) 58105–58112.
[93] Y. Zhao, N. Kornienko, Z. Liu, et al., J. Am. Chem. Soc. 137 (2015) 2199–2202.
[94] M. Meyn, K. Beneke, G. Lagaly, Inorg. Chem. 32 (1993) 1209–1215.
[95] D.T. Lee, J.D. Jamir, G.W. Peterson, et al., Small 15 (2019) e1805133.
[96] Y. Yu, X.J. Wu, M. Zhao, et al., Angew. Chem. Int. Ed. 56 (2017) 578–581.
[97] A. Huang, Y. Chen, N. Wang, et al., Chem. Commun. 48 (2012) 10981–10983.
[98] Z. Dai, L. Bai, K.N. Hval, et al., Sci. China Chem. 59 (2016) 538–546.
[99] C. Guo, Y. Jiao, Y. Zheng, et al., Chem 5 (2019) 2429–2441.
[100] F. Sun, G. Wang, Y. Ding, et al., Adv. Energy Mater. 8 (2018) 1800584.
[101] X. Liu, T. Yue, K. Qi, et al., Chin. Chem. Lett. 31 (2020) 2189–2201.
[102] Y.T. Guntern, J.R. Pankhurst, J. Vavra, et al., Angew. Chem. Int. Ed. 58 (2019) 12632–12639.
[103] L.C. Seitz, C.F. Dickens, K. Nishio, et al., Science 353 (2016) 1011–1014.
[104] R. Subbaraman, D. Tripkovic, K.C. Chang, et al., Nat. Mater. 11 (2012) 550–557.
[105] Y.H. Xiao, W. Tian, S. Jin, et al., Small 16 (2020) 2005111.
[106] J.D. Benck, T.R. Hellstern, J. Kibsgaard, et al., ACS Catal. 4 (2014) 3957–3971.
[107] Y. Guo, X. He, Y. Su, et al., J. Am. Chem. Soc. 143 (2021) 5755–5762.
[108] S.Z. Hou, X.D. Zhang, W.W. Yuan, et al., Inorg. Chem. 59 (2020) 11298–11304.
[109] C. Yang, S. Li, Z. Zhang, et al., Small 16 (2020) 2001847.
[110] A. Dhakshinamoorthy, H. Garcia, Chem. Soc. Rev. 41 (2012) 5262–5284.
[111] R. Yan, Y. Zhao, H. Yang, et al., Adv. Funct. Mater. 28 (2018) 1802021.
[112] P. Li, H. Zhan, S. Tian, et al., ACS Appl. Mater. Interfaces 11 (2019) 13624–13631.
[113] Y. Ma, H. Zhao, P. Yu, et al., Sci. China Ser. B 52 (2009) 741–745.
[114] H. Hosseini, H. Ahmar, A. Dehghani, et al., Biosens. Bioelectron. 42 (2013) 426–429.
[115] F. Su, S. Zhang, H. Ji, et al., ACS Sens. 2 (2017) 998–1005.
[116] Y. Liu, S. Zhu, Z. Gu, et al., Chin. Chem. Lett. (2021), doi:10.1016/j.cclet.2021.04.023.
[117] S.P. Mezyk, T. Helgeson, S.K. Cole, et al., J. Phys. Chem. A 110 (2006) 2176–2180.
[118] W.C. Hu, M.R. Younis, Y. Zhou, et al., Small 16 (2020) e2000553.
[119] D.E.J.G.J. Dolmans, D. Fukumura, R.K. Jain, Nat. Rev. Cancer 3 (2003) 380–387.
[120] S.M. Wei, K. Feng, C. Li, et al., Matter 2 (2020) 495–506.
[121] C. Ji, Q. Gao, X. Dong, et al., Angew. Chem. Int. Ed. 57 (2018) 11384–11388.

[122] B. Gu, W. Wu, G. Xu, et al., Adv. Mater. 29 (2017) 1701076.
[123] Z. Gao, Y. Li, Y. Zhang, et al., ACS Appl. Mater. Interfaces 12 (2020) 1963–1972.
[124] D.-W. Lim, H. Kitagawa, Chem. Soc. Rev. 50 (2021) 6349–6368.
[125] Y. Qin, J. Guo, M. Zhao, Trans. Tianjin Univ. 27 (2021) 434–449.
[126] Y. Guo, Z. Jiang, W. Ying, et al., Adv. Mater. 30 (2018) 1705155.
[127] J. Troyano, O. Castillo, J.I. Martínez, et al., Adv. Funct. Mater. 28 (2018) 1704040.
[128] A. Mukhopadhyay, V.K. Maka, G. Savitha, et al., Chem 4 (2018) 1059–1079.